Improving Spectral-Based Endmember Finding by Exploring Spatial Context for Hyperspectral Unmixing

Shaohui Mei [ID], *Member, IEEE*, Ge Zhang, Jun Li [ID], *Senior Member, IEEE*, Yifan Zhang [ID], *Member, IEEE*, and Qian Du [ID], *Fellow, IEEE*

Abstract—Hyperspectral unmixing, which intends to decompose mixed pixels into a collection of endmembers weighted by their corresponding fraction abundances, has been widely utilized for remote sensing image exploitation. Recent studies have revealed that spatial context of pixels is important complemental information for hyperspectral image processing. However, many well-known endmember finding (EF) algorithms identify spectrally pure spectra from hyperspectral images according to spectral information only, resulting in limited accuracy of hyperspectral unmixing application since they ignore spatial distribution or structure information in the image. Therefore, in this article, several novel spatial exploiting (SE) strategies are proposed to improve the performance of the well-known spectral-based EF (sEF) algorithms by integrating spatial information. Three different spatial exploiting strategies are designed to use pixel spatial context, by which the spectral variation of pixels can be alleviated to improve the performance of hyperspectral unmixing. Specifically, in pixel domain, the pixels are linearly reconstructed using their neighbors in which the spatially derived factor to weight the importance of the spectral information is generated using local linear representation and local sparse representation, while in the feature domain, pixels are revised using dominated features of neighboring pixels in singular value decomposition. The proposed spatial exploiting strategies can not only be used as a preprocessing stage to revise pixels for sEF algorithms, but also be used as a postprocessing step to revise endmembers found via sEF algorithms. Finally, experimental results on both synthetic and real hyperspectral datasets demonstrate that the proposed SE strategies can certainly improve the performance of several well-known sEF algorithms, and obtain more accurate unmixing results than several state-of-the-art spatial preprocessing methods.

Index Terms—Endmember extraction, hyperspectral unmixing, singular value decomposition, sparse representation, spatial preprocessing, spatial postprocessing.

I. Introduction

THE development of imaging sensor technologies has made hyperspectral remote sensing data widely available, providing a large amount of detailed information about the spectral characteristics of the materials that are present in the scene [1]–[3]. However, most of the pixels acquired by hyperspectral remote sensors are composed of several inhomogeneous ground objects, which are well known as *mixed pixels* or *mixtures*. The phenomenon is caused by low spatial resolution of the sensor, which would combine distinct materials into homogenous or intimate mixture, making it difficult to separate different pure ground objects [4], [5]. The wide presence of mixtures not only influences the performance of image classification and target recognition, but also is an obstacle to quantitative analysis of hyperspectral images [6]. Therefore, spectral mixture unmixing (SMU) is proposed to solve such mixed-pixel problems for quantitative analysis of hyperspectral remote sensing images.

Generally, SMU techniques can be divided into three steps.
1) The estimation of virtual dimension that defined as the number of spectrally distinct signatures in hyperspectral data [7], [8], where several typical methods have been proposed, including Neyman–Pearson detection theory-based thresholding method (HFC) [9], noise-whitened HFC [10], hyperspectral signal identification with minimum error (HySime) [11], and etc.
2) Endmember extraction that extracts spectrally virtual signatures of ground objects or endmember finding (EF) that seeks for the hypothetically existed pure signatures.
3) Abundance estimation (AE), which expresses each image pixel in terms of linear/nonlinear combinations of spectral signatures, known as fully constrained least squares method [12], multichannel Hopfield neural network [13], and etc.

Selecting an appropriate endmember set plays an extremely important role in SMU since the ultimate aim of SMU is to provide an accurate composition of ground objects and a poorly constructed endmember set leads to incorrect interpretations.

Over the decades, many algorithms have been developed for automatic or semiautomatic finding of spectral endmembers [14]. By assuming the presence of pure pixels in the image, many EF algorithms aim to identify endmembers directly from the image, such as orthogonal subspace projection (OSP) algorithm

[15], pixel purity index algorithm [16], N-FINDR algorithm [17], automatic target generation process (ATGP) [18], vertex component analysis (VCA) [19], and simplex growing algorithm [20]. However, when such pure-pixel assumption does not hold, virtual endmembers, which are not necessarily present in the pixel set comprised of input data samples, are extracted by adopting an optimization strategy. The minimum volume assumption [21] has been widely utilized to extract such virtual endmembers by determining a simplex of minimum volume enclosing the data, such as the minimum volume simplex analysis [22], and minimum-volume enclosing simplex [23].

In addition, many blind unmixing algorithms are proposed to extract virtual endmembers by performing EF and AE iteratively, such as minimum volume constrained NMF [24], minimum end-memberwise distance constrained NMF (MewDC-NMF) [25], minimum dispersion constrained NMF [26], sparse constrained NMF algorithms [27], [28], robust collaborative NMF algorithm [29], deep NMF algorithms [30], to name a few. Other linear unmixing methods based on nonnegative projection [31], convex geometric approach [32], [33] and collaborative sparse [34] have also been well developed. All of these EF algorithms identify endmembers according to the spectral only, which denoted as spectral-based EF (sEF) algorithms.

Due to the inevitable presence of spectral variation in hyperspectral images, unmixing results based on the endmembers identified in the sEF algorithms may be of limited accuracy [35]. In order to achieve better performance in SMU, many spatial-spectral-based EF algorithms are proposed to extract endmembers by taking both spatial distribution and spectral discrimination into account, such as automated morphological endmember extraction (AMEE) algorithm [36], the spatial-spectral endmember extraction tool [37], and spatial purity-based endmember extraction (SPEE) algorithm [35]. It has been demonstrated that the performance of spatial-spectral-based EF algorithms clearly outperforms that of traditional sEF algorithms.

Recently, the performance of traditional sEF algorithms is improved by exploiting spatial information at a preprocessing stage. Many spatial preprocessing methods have been proposed for this purpose [38]–[44], which can be categorized into two groups. The first one alleviates the influence of spectral variation on a specific pixel by smoothing the spectra using its neighbors, such that a modified simplex is formed, using not only the spectral signature but also spatial information [38]. However, its performance is generally sensitive to noise. The second group refines original pixel set to a small subset for sEF by integrating spatial and spectral information [39]–[44]. Such preprocessing algorithms can reduce the computational load of successive sEF algorithms, as well as improving the accuracy of EF. However, they tend to neglect small targets or anomalous areas that may be present in the image, and guide the subsequent sEF algorithm to homogenously mixed areas that do not contain pure pixels.

In this article, several novel spatial exploiting (SE) strategies are proposed as a preprocessing or postprocessing step for the sEF algorithms. In the pixel domain, similar to SPP algorithm [38], each pixel in a hyperspectral image is modified by exploiting its spatial context. Specifically, in this article, the spatially derived factor to weight the importance of spectral information is generated conveniently, instead of the complex parameterized scalar factor generation in [38]. Moreover, spectral variation within a local spatial neighborhood is also alleviated in the feature domain by reconstructing pixels using dominated features. Particularly, three SE algorithms, which are based on singular value decomposition (SVD), local linear representation (LLR), and local sparse representation (LSR), are designed. More importantly, the proposed SE algorithms are utilized as either a preprocessing step or postprocessing step for the traditional sEF algorithms. Geometric interpretation is further conducted for the proposed SE algorithms as a preprocessing and postprocessing step for sEF algorithms. Finally, experimental results over both synthetic and real hyperspectral datasets indicate that, our proposed SE strategies can improve the performance of sEF algorithms in both preprocessing and postprocessing manner. Moreover, compared with other available strategies for spatial preprocessing, the anomalous endmembers can be well preserved by the proposed SE strategies for further spectral mixture analysis.

The remainder of this article is organized as follows. Section II proposes the spatial context exploiting techniques, and their preprocessing combination and postprocessing combination with existing sEF algorithms. Experimental results on both synthetic and real hyperspectral datasets are reported in Section III. Finally, Section IV concludes this article with some remarks.

II. PROPOSED METHOD

In a hyperspectral image, spectral information treats a pixel as an individual unit, which is independent of its neighboring pixels, while spatial distribution accounts for the correlation between pixels and their neighbors. The sEF algorithms ignore the spatial distribution of pixels when finding endmember for SMU, which means the data are not handled as an image but as an unordered list of spectral signatures [36]. It has been demonstrated that in the spatial-spectral-based EF algorithms spatial information is helpful to alleviate the influence of spectral variation and, thus, improve the performance of sEF [35], [36]. Therefore, in this article, spatial information is exploited a prior or *a posteriori* to improve their performance.

A. SE Strategies

According to the linear mixture assumption, pixels in a hyperspectral image often fall into a simplex determined by endmembers. Therefore, the intrinsic dimensionality of hyperspectral data are much lower than its observed dimensionality defined by the number of bands, indicating that the subspace other than the simplex is occupied by spectral variation and noises. If the hyperspectral data are projected to its intrinsic signal space, the influence of spectral variation and noises can be alleviated.

On the other hand, classical sEF algorithms only explore spectral information but do not adequately incorporate spatial information into hyperspectral images. Using spatial information can alleviate the influence of spectral variation and, thus,

improve the performance of unmixing. Therefore, in this article, each pixel is refined by its spatially neighboring pixels or in the feature domain. In order to alleviate the spectral variation within pixels, LLR, and LSR are used to revise pixels in the pixel domain by assuming that pixels can be linearly reconstructed by some of their neighboring pixels, while SVD is used to extract dominated features of the spatial neighborhood around pixels to revise pixels in feature level by assuming that nondominated features account for spectral variance and noises [45].

1) LLR-Based SE Strategy: Recent studies have shown that many real-world data is actually sampled from a nonlinear low-dimensional manifold which is embedded in a high-dimensional ambient space [46]. Therefore, each pixel in an image together with pixels in its spatial neighborhood (SN) are expected to lie on or close to a locally linear patch of the manifold. By characterizing such local geometry of these patches, each pixel can be linearly reconstructed by pixels in its SN. Let $\mathbf{r} = (r_1, r_2, \ldots, r_b)^T$ represents a b-band pixel in a hyperspectral image. The coefficients that reconstruct pixel $\mathbf{r}$ by its neighboring pixels can be obtained by the following minimization problem:

$$\mathbf{w} = \arg\min_{\mathbf{w}} \sum_{\mathbf{r}_j \in SN(\mathbf{r})} \left\| \mathbf{r} - \sum_j \mathbf{w}_j \mathbf{r}_j \right\|^2 \tag{1}$$

in which $\mathbf{r}_j$ represents the jth neighbor pixel in $SN(\mathbf{r})$ and the weight $\mathbf{w}_j$ represents the contribution of $\mathbf{r}_j$ to the reconstruction of $\mathbf{r}$. As for $\mathbf{w}$, it is a vector composed of weight $\mathbf{w}_j$, which just like the spatially derived factor to weight the importance of the spectral information of neighbor pixels. Since the noises can be alleviated by characterizing such locally linear patch to reconstruct pixels, we can implement SE by reconstructing pixel $\mathbf{r}$ according to LLR as

$$\hat{\mathbf{r}} = \mathbf{N} \cdot \mathbf{w} \tag{2}$$

in which $\hat{\mathbf{r}}$ represent the revised version of pixel $\mathbf{r}$, $\mathbf{N} \in \mathcal{R}^{b \times p}$ represents all the pixels in the spatial neighborhood of pixel $\mathbf{r}$, and p denotes the number of pixels in the spatial neighborhood. By replacing $\mathbf{r}$ with $\hat{\mathbf{r}}$, the performance of sEF and even unmixing can be improved since local spectral variation is alleviated using spatial context of pixels.

2) LSR-Based SE Strategy: Sparse representation has been developed in many fields [47]–[49], and it has also received some attention in the field of unmixing. Generally, pixels of homogeneous components are most likely present in neighboring areas. Therefore, if a pixel is reconstructed by its neighboring pixels that own homogeneous components, the local spectral variation can be alleviated. However, pixels in a spatial neighborhood may belong to heterogeneous categories, indicating that pixels of homogeneous components may be sparsely present in a spatial neighborhood. In order to alleviate the influence of local spectral variation over SMU problems, sparse representation is used to improve spectral signature of a pixel using its neighboring pixels.

The main idea of the LSR-based strategy is to find the optimal sparse representation of each input pixel by its spatial neighbors.

Therefore, the LSR of pixel $\mathbf{r}$ can be formulated as

$$\mathbf{v} = \arg\min_{\mathbf{v}^*} \frac{1}{2} ||\mathbf{r} - \mathbf{N}\mathbf{v}^*||_2^2 + \lambda ||\mathbf{v}^*||_1 \tag{3}$$

while $\mathbf{v}$ represents a sparse vector of their corresponding weights and λ is a regularization parameter. The first term in (3) represents that pixel $\mathbf{r}$ can be linearly reconstructed by its neighboring pixels while the second term in (3) guarantees a sparse reconstruction that only selects pixels of homogeneous components for representation. In this article, the L1 Homotopy MATLAB Toolbox [50], which is available online,[1] is used to solve the representation coefficient $\mathbf{v}$. Consequently, in the proposed LSR-based strategy, pixel $\mathbf{r}$ can be refined as

$$\hat{\mathbf{r}} = \mathbf{N} \cdot \mathbf{v}. \tag{4}$$

3) SVD-Based SE Strategy: In order to exploit its spatial context, all the pixels in its spatial neighborhood are taken into account. The SVD of pixels in a spatial neighborhood $\mathbf{N}$ is defined as [51]

$$\mathbf{N} = \mathbf{S} \cdot \mathbf{V} \cdot \mathbf{D} \tag{5}$$

where $\mathbf{D} \in \mathcal{R}^{p \times p}$ contains the unit row eigenvectors of $\mathbf{N}^T\mathbf{N}$ sorted in descending significance, $\mathbf{S}$ is a $b \times b$ matrix containing the unit column eigenvectors of $\mathbf{N}\mathbf{N}^T$, and $\mathbf{V} \in \mathcal{R}^{b \times p}$ is of the following form:

$$\mathbf{V} = \begin{pmatrix} V_{11} & \cdots & 0 \\ \vdots & \ddots & \vdots \\ 0 & \cdots & V_{pp} \\ \vdots & \ddots & \vdots \\ 0 & \cdots & 0 \end{pmatrix} \tag{6}$$

with $V_{ii}(i = 1, 2, \ldots, p)$ being the square roots of nonzero eigenvalues of $\mathbf{N}^T\mathbf{N}$ sorted in descending order.

It has been pointed out that the greater singular vectors come about as a result of endmembers while the smaller singular vectors come about as a result of the noise such as spectral variation, measurement error, and etc. [51], [52]. Therefore, if we can discriminate the singular vectors responsible for endmembers, the influence of noises and spectral variation on pixels can be alleviated by only utilizing singular vectors of endmembers. Since the importance of singular vectors is represented by their corresponding eigenvalues, the number of singular vectors for endmembers is identified as

$$q = \arg\min_k \frac{\sum_{i=1}^k V_{ii}}{\sum_{i=1}^p V_{ii}} < T_{\text{SVD}} \tag{7}$$

where T_{SVD} is a threshold. As a result, the first q singular vectors come as a result of endmembers, and thus, a revised data matrix is reconstructed as

$$\hat{\mathbf{N}} = \mathbf{S} \cdot \hat{\mathbf{V}} \cdot \mathbf{D} \tag{8}$$

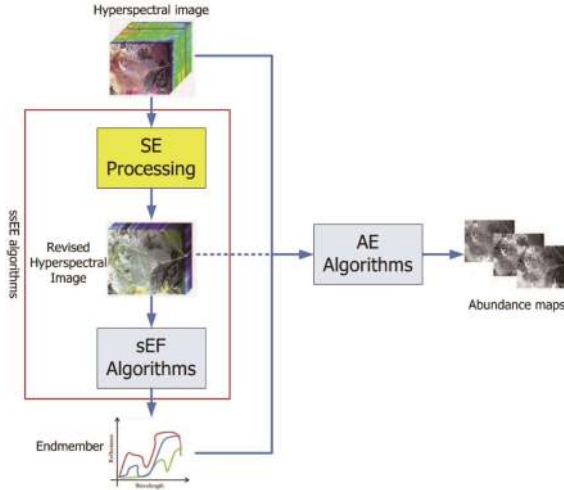[1] https://intra.ece.ucr.edu/ sasif/homotopy/

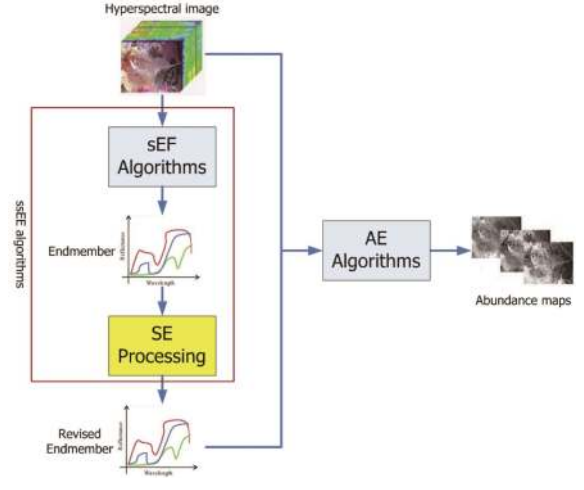Fig. 1. Flowchart of SMU by using the proposed SE strategies as a preprocessing stage.

Fig. 2. Flowchart of SMU by using the proposed SE strategies as a postprocessing step.

where $\hat{\mathbf{V}}$ is determined as

$$\hat{\mathbf{V}} = \begin{pmatrix} V_{11} & \cdots & 0 & \cdots & 0 \\ \vdots & \ddots & \vdots & \cdots & \vdots \\ 0 & \cdots & V_{qq} & \cdots & 0 \\ 0 & \cdots & 0 & \cdots & 0 \\ \vdots & \ddots & \vdots & \cdots & \vdots \\ 0 & \cdots & 0 & \cdots & 0 \end{pmatrix}. \tag{9}$$

According to (8), the spatial context can be exploited to alleviate the influence of spectral variation and noises on pixels.

B. Implementing Spatial Information Into sEF Algorithms

1) Preprocessing by the SE Strategy: According to the proposed SE strategy, the influence of spectral variation and noises on single pixels can be alleviated. Thus, a refined hyperspectral image can be obtained by implementing the proposed SE strategies pixel-by-pixel. As a result, the performance of traditional sEF algorithms can be improved by implementing them on such revised hyperspectral data. The flowchart of adopting the proposed SE algorithms as a preprocessing step for SMU is shown in Fig. 1. Similar to the SPP algorithm [38], the proposed SE algorithms are directly performed on the original hyperspectral image to alleviate the influence of spectral variation and noises. Traditional sEF algorithms are then implemented on the revised hyperspectral image to find endmembers. The combination of the preprocessing by SE and sEF (shown in the red rectangular in Fig. 1) can be viewed as a spatial-spectral-based EF algorithm to find endmembers. In such way, the performance of traditional sEF algorithms can be improved by considering spatial context. Finally, the AE algorithms are adopted to estimate abundance maps for endmembers. It should be noted that the AE algorithms can be implemented on either the original or the revised hyperspectral image.

2) Postprocessing by the SE Strategy: The proposed SE algorithms can also be implemented as a postprocessing step to improve the performance of traditional sEF algorithms. As shown in Fig. 2, the proposed SE algorithms are performed after the endmember finding step by the sEF algorithms. Under such circumstance, only the spatial context of the found endmembers are exploited. Thus, the performance of traditional sEF algorithms can also be improved. Similarly, the combination of sEF and postprocessing by SE (shown in the red rectangular in Fig. 2) can be viewed as a spatial-spectral-based EF algorithm to find endmembers. Since the number of pixels to be revised by SE in postprocessing is much smaller than that in preprocessing, the computation complexity of the proposed SE strategies as a postprocessing step is much lower than that as a preprocessing step. Finally, the AE algorithms are adopted to estimate abundance maps for the revised endmembers.

3) Geometric Illustration: Fig. 3 shows a geometric interpretation of the proposed SE algorithms as a preprocessing and postprocessing step for SMU. According to geometric analysis of hyperspectral images in previous studies [53], [54], all the pixels in an image fall into a simplex whose vertexes are determined by endmembers. As shown in Fig. 3(a), in a 2-D space, all the pixels (denoted as blue solid dots) fall into a triangle determined by endmember 1, 2, and 3. In the preprocessing steps, all the pixels are revised pixel-by-pixel by exploiting their spatial context through SE-LLR, SE-LSR, or SE-SVD. And then EF step is applied to the revised image. As a result, all the revised pixels (denoted as red solid dots) fall into a new triangle determined by endmember $7'$, $4'$, and $3'$. The revised versions of original endmembers may not be the vertexes of the new triangle, indicating that the pixels to be endmembers vary after preprocessing by the SE algorithms. However, as shown in Fig. 3(b), the nonendmember pixels remain the same when SE strategies are adopted as a postprocessing step. Under such circumstance, the proposed SE algorithms are performed after the EF step by the sEF algorithms, where only the spatial
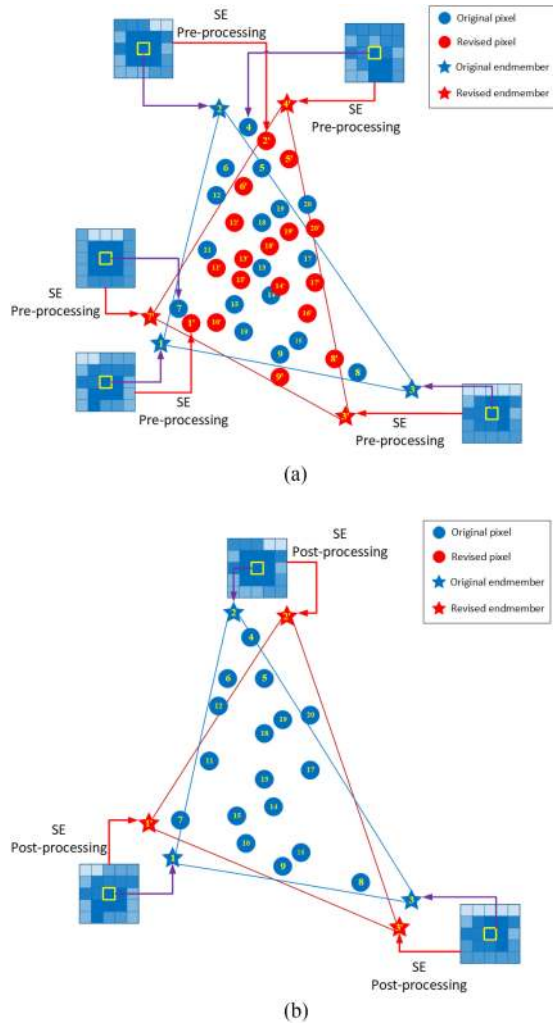
(a)

(b)

Fig. 3.   Geometric interpretation of the proposed SE strategies for: (a) prepro-cessing; (b) postprocessing.

context of the found endmembers are exploited to revised the endmembers. The new simplex (triangle $1' - 2' - 3'$) can be viewed as a revised version of the original simplex that enclosing the pixels (triangle $1 - 2 - 3$).

C. Improvement Over Anomalous Endmembers

Similar to many existing spatial-spectral-based EF algorithms (such as AMEE [36] and SPEE [35]) and the SPP algorithm [38], when our proposed SE algorithms are adopted as a preprocessing step for sEF, the combined spatial-spectral-based EF algorithm penalizes the selection of anomalous pixels and increases the probability of selecting the majority of pixels that are homogeneous in nature. Even if the proposed SE strategies are adopted in postprocessing that does not influence the finding of anomalous endmembers by the sEF algorithms, the spectral signature of anomalous endmembers may be smoothed excessively by its inhomogeneous neighboring pixels. In order to solve this problem, the proposed SE step can be turned ON or OFF by checking the spectral similarity between pixels $\mathbf{r}$ and its spatially revised
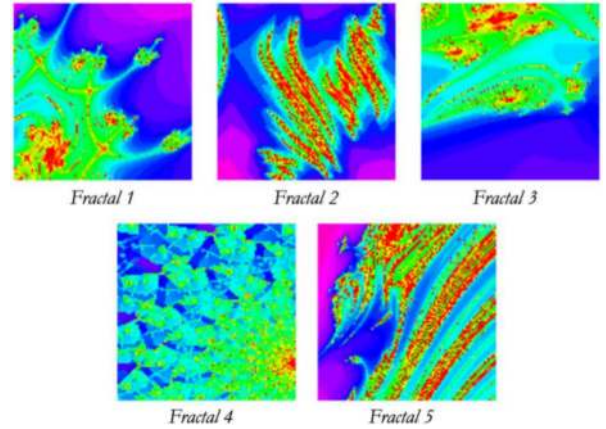

Fig. 4.   Five synthetic images used in experiments, where spatial patterns were generated using fractals.

signature $\hat{\mathbf{r}}$, which can be formulated as follows:

$$\hat{\mathbf{r}} = \begin{cases} \mathbf{r}, & \text{if } \text{SAD}(\mathbf{r}, \hat{\mathbf{r}}) > T \\ \hat{\mathbf{r}}, & \text{if } \text{SAD}(\mathbf{r}, \hat{\mathbf{r}}) \leq T \end{cases} \quad (10)$$

where $\text{SAD}(\mathbf{r}, \hat{\mathbf{r}})$ is the spectral angle distance (SAD) between $\mathbf{r}$ and $\hat{\mathbf{r}}$ and T is an adjustable threshold. When the revised pixel is significantly different from its original pixel, we believe there are abnormal pixels in its spatial neighborhood or the current pixel is the abnormal one. Then, our proposed SE strategies would choose to turn OFF the revision of the current pixel.

III. EXPERIMENTS

In this section, extensive experiments are conducted to verify the performance of the proposed SE strategies as a preprocessing or postprocessing step for several well-known sEF algorithms, including OSP [15], N-FINDR [17], ATGP [18] algorithms, and VCA [19]. For that purpose, we test the same set of algorithms with and without spatial preprocessing (so-called "ORI"). Several state-of-the-art spatial preprocessing algorithms are adopted for comparison, including SPP [38], RBSPP [39], SSPP [40], and RCSPP [44]. Meanwhile, one typical spatial-spectral-based EF algorithm, i.e., SPEE algorithm [35], is also selected. All experimental results in this section are the average of 10 random tests.

A. Datasets

1) Synthetic Dataset: The dataset of five 100×100-pixel synthetic hyperspectral scenes that used in [40] is adopted in this experiment. These images are simulated using spectra of minerals from a spectral library compiled by the U.S. Geological Survey (USGS)[2] under linear mixture assumption, shown in Fig. 4. In all the five synthetic images, the number of endmembers is fixed as $p = 9$. Moreover, zero-mean Gaussian noise was added in order to simulate contributions from ambient (clutter) and instrumental sources by following the procedure described in [15]. As a result, the signal-to-noise ratio (SNR) of
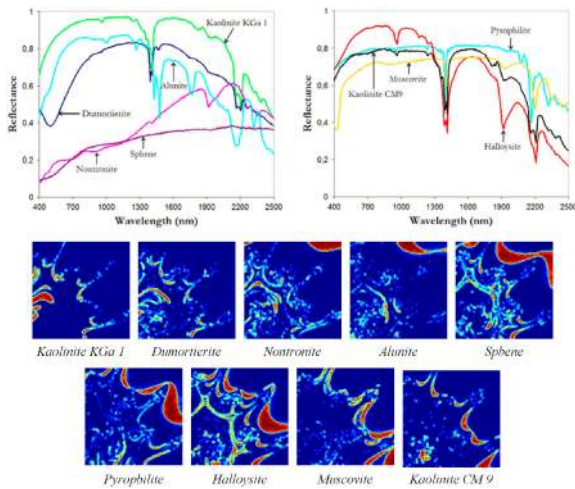
[2]http://speclab.cr.usgs.gov/spectral.lib06

Fig. 5. USGS library signatures used in the synthetic dataset labeled as "Fractal 1" and the abundance maps associated to each reference USGS signatures [40].

the synthetic dataset is varied from $10 : 1$ to $70 : 1$. Specially, the nine spectra from the USGS spectral library that is used to simulate a scene labeled as "Fractal 1", together with their corresponding abundance maps are shown in Fig. 5. Note that the fractional abundances in each pixel of the dataset are positive and add up to unity, ensuring that all pixel instances in the synthetic fractal image strictly adhere to a fully constrained linear mixture model.

2) Cuprite Dataset: The well-known AVIRIS dataset over the Cuprite areas in Nevada, USA,[3] which has 224 channels ranging from 370 to 2510 nm with a ground instantaneous field of view of 20 m, is used in this experiment. This dataset has been widely used to validate the performance of endmember finding algorithms. The cropped image corresponds to a 350×350 pixel subset of the sector labeled as $f970619t01p02_r02_sc03.a.rfl$ in the online data. In this experiment, only 186 reflectance bands are adopted after removing bands $1 - 4, 105 - 115, 150 - 170$, and $223 - 224$ due to water absorption and low SNR in those bands. The Cuprite site is well understood mineralogically, and has several exposed minerals of interest included in the USGS spectral library. A few selected spectra from the USGS library, corresponding to highly representative minerals in the Cuprite mining district, are utilized as ground-truth spectra to substantiate endmember signature purity, including Alunite, Andradite, Buddingtonite, Dumortierite, Jarosite, Kaolinite, Montmorillonite, and Muscovite. For the number of endmembers, the HySime [11] provided an estimation of 16, as same as that by HFC [9] method using the input false-alarm probability $P_F = 10^{-5}$.

3) Urban HYDICE Dataset: The second real-world dataset is the Urban HYDICE[4] hyperspectral image. The image is of size 307×307 over 210 spectral channels, with a spectral resolution of 10 nm covering a spectral range from 400 to 2500 nm.

[3]http://aviris.jpl.nasa.gov/html/aviris.freedata.html
[4]http://www.erdc.usace.army.mil/Media/Fact-Sheets/Fact-Sheet-Article-View/Article/610433/hypercube/

After low SNR bands are removed (channels $1 - 4$, 76, 87, $101 - 111$, $136 - 153$, and $198 - 210$), only 162 bands remain to be used in the experiment. The number of endmembers to be found is set to 9 in all experiments after the consensus reached between HySime [11] and the HFC [9] method, implemented using $P_F = 10^{-3}$ as the input false-alarm probability [7]. In subsequent qualitative assessment, we just adopt four distinct targets of interest, including asphalt, grass, roof, and tree.

B. Evaluation Metrics

Two quantitative metrics are adopted to evaluate the performance of our different SE strategies to improve well-known sEF algorithms. The first metric is the SAD values (in degrees) between the found endmembers and their ground-truth spectral signatures. Let $\hat{\mathbf{E}}_k$ be a found endmember and $\mathbf{E}_k$ be the most similar spectral signature in the USGS library. The SAD between two spectral signatures is defined as

$$\text{SAD}(\hat{\mathbf{E}}_k, \mathbf{E}_k) = \arccos\left(\frac{\hat{\mathbf{E}}_k \cdot \mathbf{E}_k}{\|\hat{\mathbf{E}}_k\|\|\mathbf{E}_k\|}\right) \qquad (11)$$

in which $\| \cdot \|$ represents the magnitude of vectors. Note that low SAD scores mean high spectral similarity between the compared vectors. This spectral similarity measure is invariant in the multiplication of $\mathbf{e}$ and $\hat{\mathbf{e}}$ by constants and, consequently, is invariant before unknown multiplicative scalings that may arise due to differences in illumination and angular orientation.

Further for quantitatively evaluating the performance of our proposed SE algorithms on real-world data experiments, the pixel reconstruction error (ReconEr), evaluated by the root-mean-square error (RMSE) between the original b-band pixel $\mathbf{r}$ and its reconstructed version using the unmixing results $\hat{\mathbf{r}}$, which is defined as

$$\text{ReconEr}(\mathbf{r}, \hat{\mathbf{r}}) = \frac{1}{b}\sum_{i=1}^{b}(r_i - \hat{r}_i)^2. \qquad (12)$$

C. Parameter Analysis

First of all, the impact of parameters, including λ for SE-LSR, T for SE-SVD, and window size w_s for all three SE strategies, are discussed through several sets of simulated experiments.

1) w_s for SE-LLR: As the only parameter in the proposed LLR-based SE strategy, we analyzed the impact of the window size w_s considering 8-connected (3×3 window), 24-connected (5×5 window), and 48-connected (7×7 window). The upper part of Fig. 6 lists the results of proposed SE-LLR as a preprocessing step for different sEF algorithms. It is observed that, the proposed SE-LLR does not vary much when different window size is selected. Therefore, in the following experiment, w_s is set as 3 for low computational complexity.

2) w_s and λ for SE-LSR: With regard to the proposed LSR-based SE strategy, the impacts of w_s and regularization parameter λ in (3) are also analyzed by varying w_s as [3, 5, 7] and λ from 10^2 to 10^6. The average performance of proposed SE-LSR with different parameters for different sEF algorithms is shown in the middle of Fig. 6. It is observed that when $w_s = 7$, the
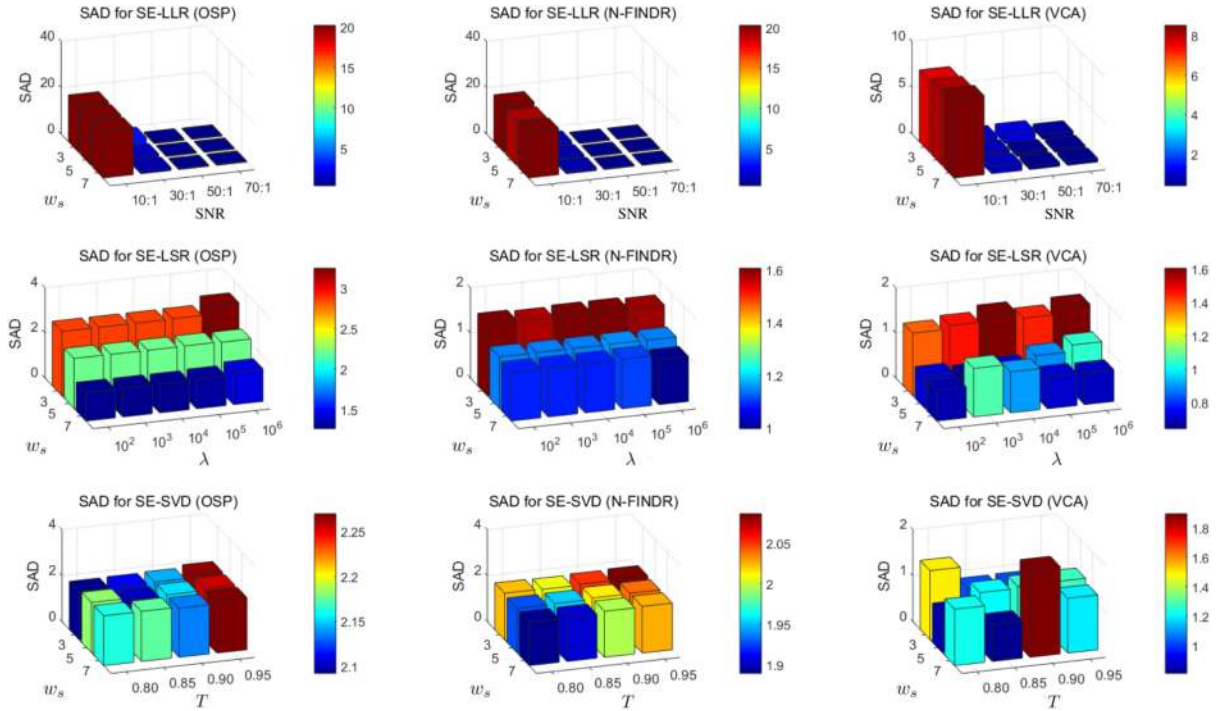
Fig. 6. Parameter analysis of the proposed SE algorithms through several sets of simulated experiments, including w_s for all three SEs, λ for SE-LSR, and T for SE-SVD.

value of SAD is almost at the lowest position in most cases. As for λ, SAD may achieve a lower value when it is set as 10^3.

3) w_s and T for SE-SVD: In the proposed SVD-based SE strategy, the threshold T is varied from 0.80 to 0.95 at intervals of 0.05 while w_s is also selected as [3, 5, 7]. The lower part of Fig. 6 intuitively displays the subtle effect of mutative parameters on the unmixing performance. It is observed that SVD under $w_s = 5$ and $T = 0.90$ is less sensitive to noises and always able to maintain better performance.

D. Experiments Using Synthetic Dataset

1) Preprocessing by Proposed SE Strategies: In this experiment, all of the three SE strategies, including LLR, LSR, and SVD, are considered. Table I shows the average SAD scores (in degrees) between the ground-truth signatures and their corresponding found endmembers preprocessed by different algorithms over synthetic dataset with different SNRs. It is observed that, the combination of the proposed SE strategies with the sEF algorithms generally provides better results (lower spectral angles) over both the original version of sEF algorithms and the state-of-the-art spatial preprocessing algorithms. It is worthy to be noted that due to the absence of pure endmembers in this synthetic dataset, the performance of pure pixel-based SPEE is limited to some extent. In general, the improvement of our proposed SE strategies is especially obvious when SNR level is low, which means that the proposed SE strategies reduce noise and variability of pixels in a local level. However, when the SNR level is high, e.g., 70 dB, the original version of sEF algorithms can achieve satisfying results. Under such circumstances,

the spatial preprocessing strategies cannot further improve the performance of sEF. On the contrary, they may oversmooth the endmembers. Specifically, as for the three proposed SE strategies, the SE-LLR achieves excellent performance among all the considered algorithms when SNR at 10 dB while SE-LSR provides comparative results under the SNR level of 30 dB and 50 dB. Although the performance of SE-SVD is slightly worse than the other two, it is still better than SPP [38], which also aims to alleviate local spectral variation using spatial context.

2) Extracting Anomalous Endmembers: In order to test the ability of proposed SE algorithms of selecting abnormal endmembers, we randomly select 10 spectral features from the USGS spectral library (excluding those used in synthetic images), and replace the synthetic spectra in the 10 random nonadjacent locations with the spectra of the current ones. In this experiment, we set $w_s = 3$, SNR= 30 :1. Since VCA sometimes cannot find the required number of endmembers in this case, it is not considered further. Table II lists the probability value of successfully reserving abnormal endmembers by various spatial preprocessing SE strategies. It is observed that our three proposed SE-based preprocessing strategies clearly outperform other spatial preprocessing strategies in extracting anomalous endmembers, which is even better than the original version of sEF algorithms. This is because the anomalous endmembers are not smoothed by turning OFF the SE processing according to (10) in the proposed SE strategies. However, those clustering-based preprocessing algorithms, like SSPP and RCSPP, would penalize the selection of anomalous endmembers.

3) Postprocessing by Proposed SE Strategies: In this section, our proposed SE strategies (SE-LLR, SE-LSR, and SE-SVD)

TABLE I

AVERAGE SAD SCORES (IN DEGREES) BETWEEN THE GROUND-TRUTH SIGNATURES AND CORRESPONDING FOUND ENDMEMBERS BY DIFFERENT PREPROCESSING SE ALGORITHMS WITH DIFFERENT SNRs. THE BEST RESULTS OF SPECIFIC SNR FOR A GIVEN sEF ALGORITHM ARE IN BOLDED WHILE THE SUBOPTIMAL RESULTS ARE UNDERLINED

	Algorithm	SNR=10:1	SNR=30:1	SNR=50:1	SNR=70:1
NFINDR	ORI	19.519	2.093	<u>0.464</u>	**0.384**
	SPP	<u>11.690</u>	2.293	<u>0.778</u>	0.701
	RBSPP	27.331	2.135	0.648	0.574
	SSPPR	27.770	2.089	0.538	0.403
	RCSPP	20.692	2.654	1.512	1.613
	SE-LLR	**8.634**	<u>1.413</u>	0.467	0.401
	SE-LSR	19.809	**1.087**	**0.394**	<u>0.390</u>
	SE-SVD	20.718	2.014	0.466	0.412
OSP	ORI	20.189	2.118	<u>0.452</u>	**0.350**
	SPP	<u>11.785</u>	2.342	<u>0.622</u>	0.536
	RBSPP	21.213	2.182	0.638	0.948
	SSPP	18.899	<u>2.107</u>	0.520	0.384
	RCSPP	20.112	2.465	1.190	1.389
	SE-LLR	**11.498**	2.969	0.539	0.405
	SE-LSR	20.189	**1.269**	**0.401**	0.464
	SE-SVD	19.875	2.151	0.460	0.432
VCA	ORI	7.665	1.199	<u>0.426</u>	0.350
	SPP	9.388	2.271	0.455	<u>0.327</u>
	RBSPP	20.421	<u>0.831</u>	0.847	0.974
	SSPP	20.233	1.010	0.722	**0.176**
	RCSPP	11.055	2.190	1.300	2.075
	SE-LLR	**3.935**	0.882	<u>0.436</u>	0.560
	SE-LSR	7.724	**0.800**	**0.406**	0.370
	SE-SVD	<u>6.755</u>	1.308	0.539	0.646
ATGP	ORI	20.839	2.261	0.595	**0.538**
	SPP	<u>12.952</u>	9.674	5.902	5.398
	RBSPP	22.005	4.456	3.787	3.077
	SSPP	19.653	3.722	2.179	1.858
	RCSPP	20.793	2.741	1.579	2.195
	SE-LLR	**12.748**	**1.351**	<u>0.583</u>	<u>0.560</u>
	SE-LSR	20.839	<u>1.557</u>	**0.576**	0.859
	SE-SVD	20.411	2.240	0.599	0.741
SPEE		10.875	6.889	4.516	4.230

TABLE II

PROBABILITY VALUE OF SUCCESSFULLY FINDING ANOMALOUS ENDMEMBERS BY VARIOUS SPATIAL PREPROCESSING SE STRATEGIES

Algorithm	ORI	SPP	RBSPP	SSPP	RCSPP	SE-LLR	SE-LSR	SE-SVD
N-FINDR	90%	34%	14%	0%	0%	98%	**99%**	85%
OSP	80%	45%	16%	0%	0%	71%	**90%**	80%
ATGP	80%	45%	15%	0%	0%	76%	**90%**	78%

TABLE III

AVERAGE SAD SCORES (IN DEGREES) BETWEEN THE GROUND-TRUTH SIGNATURES AND CORRESPONDING FOUND ENDMEMBERS BY THE PROPOSED POSTPROCESSING SE ALGORITHMS WITH TRADITIONAL sEF ALGORITHMS. THE BEST RESULTS OF SPECIFIC SNR FOR A GIVEN sEF ALGORITHM ARE IN BOLDED WHILE THE SUBOPTIMAL RESULTS ARE UNDERLINED

	Algorithm	SNR=10:1	SNR=30:1	SNR=50:1	SNR=70:1
NFINDR	ORI	19.519	2.093	0.464	0.384
	SE-LLR	<u>9.964</u>	1.444	0.470	0.391
	SE-LSR	**9.952**	**1.112**	**0.403**	**0.381**
	SE-SVD	10.671	<u>1.126</u>	<u>0.411</u>	<u>0.381</u>
OSP	ORI	20.189	2.118	0.452	0.350
	SE-LLR	**10.257**	1.409	0.448	0.355
	SE-LSR	10.867	<u>1.103</u>	**0.389**	**0.346**
	SE-SVD	<u>10.617</u>	**1.100**	0.395	0.347
VCA	ORI	<u>7.665</u>	**1.199**	<u>0.426</u>	**0.350**
	SE-LLR	18.383	9.455	8.714	8.709
	SE-LSR	**6.911**	<u>1.812</u>	**0.402**	<u>0.411</u>
	SE-SVD	7.471	<u>2.937</u>	0.743	0.793
ATGP	ORI	20.839	2.261	0.595	0.538
	SE-LLR	20.907	<u>1.372</u>	<u>0.557</u>	**0.537**
	SE-LSR	**10.013**	**1.188**	**0.552**	<u>0.538</u>
	SE-SVD	20.624	2.189	0.582	0.765
SPEE		10.875	6.889	4.516	4.230

algorithms as both preprocessing and postprocessing steps are listed in Table IV. Two well-known sEF algorithms (N-FINDR and VCA) and a typical spatial-spectral-based EF algorithm (SPEE) are adopted in this experiment. For reference, the mean SAD values across all eight USGS signatures are also reported. It is observed that better spectral approximations can be obtained for certain minerals by the proposed SEs, mainly due to the alleviated influence of spectral variation and noise in pixels. Specifically, preprocessing SE-LLR tends to estimate individual mineral spectra more accurately, while SE-SVD performs well in reducing reconstruction error. Meanwhile, the SSPP and SPEE could also extract more similar endmembers to the truth spectra. While for the mean pixel-reconstruction error, SE-SVD clearly outperforms all the other well-known spatial preprocessing algorithms all the time. Fig. 7 further shows the spectral curves for four groups of endmember signatures estimated by several spatial preprocessing algorithms. Obviously, SE-LLR and SE-SVD are able to fit the spectral curve well in most times, which not give rise to an excessive smoothness that would lead to the loss of physical meaning towards found endmembers.

In order to further evaluate the performance of unmixing, visual results are utilized for qualitative assessment. Fig. 8 shows the corresponding ground-truth classification maps produced by Tricorder software. Based on the endmembers found by VCA algorithm, the fractional abundance maps of four main materials preprocessed by SE strategies and comparison algorithms are shown in Fig. 9. It can be found that the estimated abundance maps by the proposed preprocessing SE strategies are more similar to the distribution of the four materials in the classification maps. In addition, Fig. 10 illustrates the fractional abundance maps obtained by SE postprocessing strategies, which are in good accordance with the real endmember abundances.

are taken as a postprocessing step for traditional sEF algorithms. Table III lists the SAD performance of the proposed SE strategies as a postprocessing step for OSP, N-FINDR, VCA, and ATGP. It is also confirmed that the proposed SE strategies are very effective to alleviate spectral variation even as the postprocessing step of traditional sEF algorithms. Similarly, SE-LSR gets outstanding performance in most cases, mainly owing to its well robustness to noise. This has coincided with that when the proposed SE strategies as the preprocessing step of traditional sEF algorithms.

E. Experiments Over Cuprite Dataset

The experimental results of unmixing on the original AVIRIS Cuprite dataset and the revised images by the proposed SE

TABLE IV

AVERAGE SAD SCORES (IN DEGREES) AND AVERAGE PIXEL-RECONSTRUCTION ERROR (RECONER) OBTAINED AFTER COMPARING THE ORIGINAL AVIRIS CUPRITE DATASET WITH A RECONSTRUCTED VERSION OF THE SAME IMAGE BY THE PREPROCESSING AND POSTPROCESSING SE STRATEGIES. NOTE THAT THE BEST RESULTS OF SPECIFIC SPECTRA AND sEF ALGORITHM ARE IN BOLDED

	Algorithms	Alunite	Buddingtonite	Kaolinite	Montmorillonite	Muscovite	Jarosite	Andradite	Dumortierite	**Average SAD**	**ReconEr**
NFINDR	ORI	4.616	**3.864**	5.851	3.869	5.934	9.687	9.500	5.997	6.165	61.856
	SPP	5.827	5.107	6.724	4.478	5.707	10.682	10.286	**4.356**	6.646	61.754
	RBSPP	3.931	5.949	5.851	3.200	6.003	10.289	12.778	4.475	6.560	60.037
	SSPP	5.530	3.864	6.977	**3.094**	**4.594**	10.573	9.443	8.849	**6.115**	59.417
	RCSPP	3.443	6.231	7.029	3.401	5.524	11.078	8.887	5.200	6.349	53.385
	SE-LLR§	4.153	5.636	5.379	4.361	6.111	9.979	10.378	5.466	6.507	**45.559**
	SE-LSR§	**3.433**	4.728	**5.087**	4.079	6.113	9.689	9.441	6.951	6.190	52.652
	SE-SVD§	4.270	3.872	5.860	4.025	6.091	**9.685**	**8.235**	5.825	5.983	58.041
	SE-LLR†	4.641	4.115	5.881	3.694	5.930	9.979	9.539	5.947	6.216	61.115
	SE-LSR†	4.612	3.871	5.875	3.822	5.940	9.689	9.498	5.976	6.160	61.057
	SE-SVD†	4.700	3.869	5.858	3.831	5.939	9.702	9.496	5.984	6.172	61.521
VCA	ORI	3.906	4.852	8.568	3.945	5.970	9.583	**6.274**	5.516	6.077	51.729
	SPP	4.214	7.312	6.768	6.536	6.157	10.648	8.831	4.908	6.922	51.203
	RBSPP	4.246	5.515	**5.844**	3.240	6.079	10.448	9.504	4.444	6.165	43.925
	SSPP	6.431	4.627	7.510	**3.088**	**4.594**	10.576	9.450	**3.991**	6.283	57.060
	RCSPP	7.201	6.438	7.561	3.352	5.692	11.140	8.885	5.313	6.948	45.992
	SE-LLR§	5.958	6.565	6.815	3.466	6.181	**9.544**	10.901	4.248	6.710	39.930
	SE-LSR§	7.204	8.040	8.274	3.938	5.490	9.698	8.113	4.946	6.963	45.216
	SE-SVD§	7.433	**4.036**	8.567	4.068	6.020	9.650	8.144	4.204	6.515	38.777
	SE-LLR†	**3.868**	4.720	8.549	3.973	6.017	9.601	6.282	5.482	**6.061**	52.977
	SE-LSR†	7.874	7.392	7.074	3.955	5.364	9.591	8.145	4.269	6.708	40.212
	SE-SVD†	7.884	7.444	7.078	4.262	5.455	9.625	8.151	4.269	6.771	**39.617**
SPEE		5.356	7.863	6.679	5.415	6.075	**7.200**	**4.147**	4.666	**5.925**	58.364

§implemented as the pre-processing step.
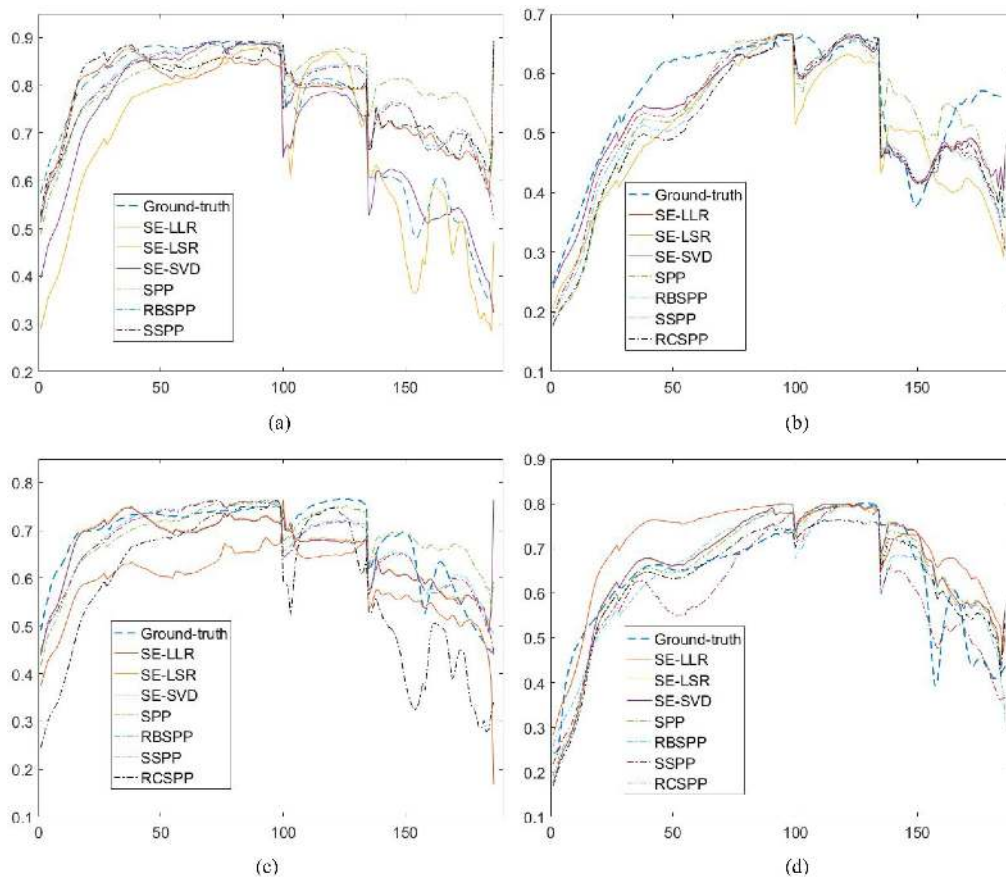
‡implemented as the postprocessing step.

Fig. 7. Comparison of the USGS library spectra with the corresponding signatures found in Cuprite dataset by different spatial preprocessing algorithms, taking (a) Alunite, (b) Buddingtonite, (c) Montmorillonite, and (d) Muscovite as an example.
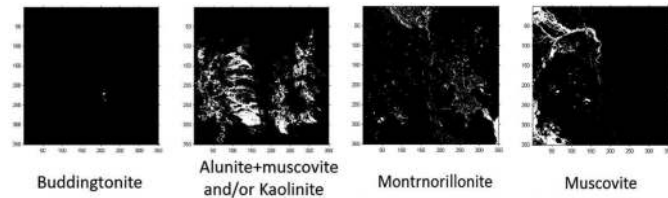
Fig. 8. Classification maps in the 350×350 pixel AVIRIS Cuprite dataset produced by the USGS Tricorder algorithm.
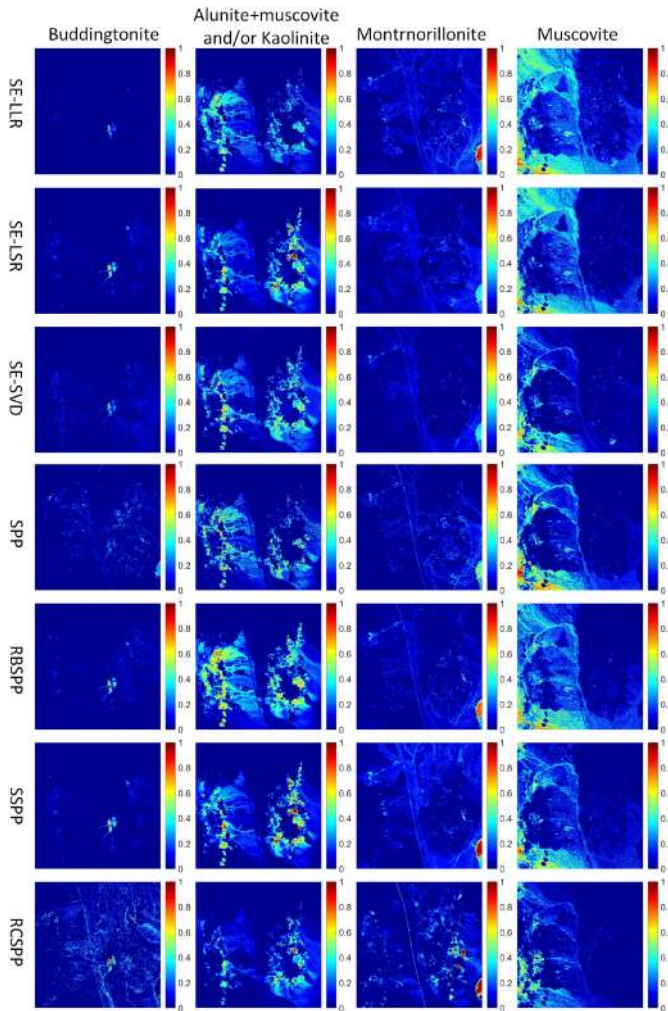

Fig. 9. Qualitative comparison of fractional abundance maps inversed by found endmembers preprocessed by SE strategies and comparison algorithms in the 350×350 pixel AVIRIS Cuprite dataset.

F. Experiments Over Urban HYDICE Dataset

Due to the lack of real-world spectra information as a prior, we only utilized visual results of abundance maps for qualitative assessment in this experiment. The corresponding referenced fractional abundance maps is shown in Fig. 11. Here, we just adopt four distinct targets of interest, including asphalt, grass, roof, and tree. In these images, the brightness of a pixel denotes the abundance of the endmember under consideration while all endmembers found by VCA algorithm. In addition, in Fig. 12, the comparison between the estimated abundance
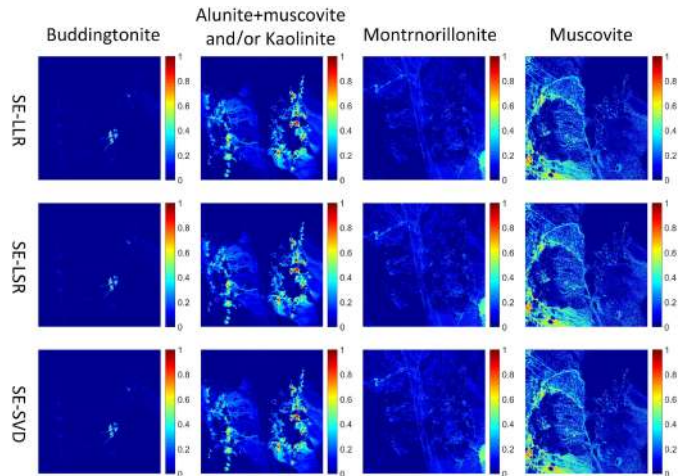

Fig. 10. Qualitative comparison of fractional abundance maps inversed by endmembers postprocessed by SE strategies in the 350×350 pixel AVIRIS Cuprite dataset.
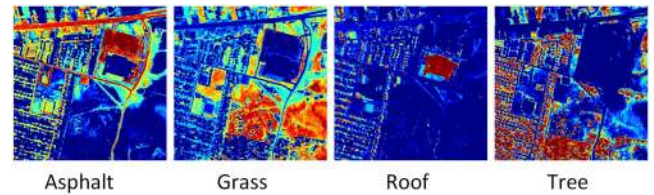

Fig. 11. Referenced fractional abundance maps of the four reference spectral signatures (asphalt, grass, roof, and tree) in the urban HYDICE hyperspectral dataset.

maps by different preprocessing algorithms is presented. It can be observed that each algorithm can obtain a reasonable abundance of most materials. Moreover, compared with other methods, the abundance maps produced by the proposed SE algorithms show better consistency. Meanwhile, the fractional abundance maps obtained by SE postprocessing strategies, shown in Fig. 13, illustrate a high degree of similarity with the reference abundances. Furthermore, the proposed SE strategies lead to a much better representation of the grass and roof endmembers when compared to the competing algorithms.

G. Computational Complexity

The computation times of different algorithms over both synthetic and real-world images are reported in Table V. In this experiment, N-FINDR algorithm is selected. The quantities are measured with Inter Core i7-6700 CPU at 3400 GHz with 12 GB of RAM using MATLAB R2016a on Windows 10 platform. In the synthetic experiments, though preprocessing SE strategies (especially LLR) take more preprocessing time than SPPs, the total computation time including AE process is almost least. This may be because endmembers preprocessed by proposed SE strategies are more closely to ground-truth spectra than other preprocessing methods so that the advantage of calculation in AE step is obvious. Due to the sparse solution of LSR, it needs more time to find endmembers in some scenarios. However, it has a

TABLE V

PREPROCESSING TIMES ANALYSIS (IN SECONDS) OVER BOTH SYNTHETIC AND REAL DATASETS WHEN N-FINDR ALGORITHM IS SELECTED FOR SEF

|	Algorithm	Synthetic data set				Cuprite data set				urban HYDICE data set			
		Pre-processing	EF time	AE time	Total time	Pre-processing	EF time	AE time	Total time	Pre-processing	EF time	AE time	Total time
NFINDR	ORI	-	3.944	73772	73776	-	36.536	139.581	176.117	-	6.566	18.058	24.624
	SPP	0.295	3.963	10834	10838	55.660	44.542	146.211	246.413	35.109	7.446	24.319	66.874
	RBSPP	0.909	4.100	9735	9740	1.694	2.824	84.292	88.81	1.649	1.913	29.086	32.648
	SSPP	1.383	3.654	14269	14274	7.063	2.969	14.887	24.919	6.406	6.079	25.604	38.089
	RCSPP	7.856	0.681	2156	2165	4.506	0.266	165.473	170.245	3.880	0.570	19.744	24.194
	SE-LLR	20.816	3.648	886	910	48.978	46.031	128.88	223.889	78.412	6.505	18.272	103.189
	SE-LSR	95.776	3.650	16378	16477	2372.500	41.259	158.481	2572.24	671.276	6.292	18.219	695.787
	SE-SVD	222.890	3.666	4145	4372	508.859	27.665	136.648	673.172	356.541	6.187	18.032	380.76
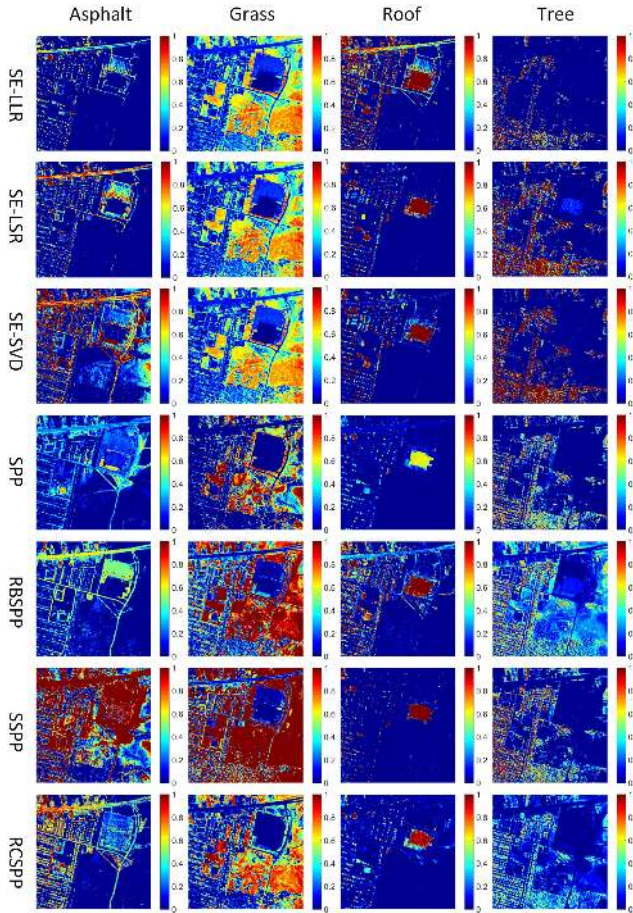
Fig. 12. Qualitative comparison between the fractional abundance maps estimated from the revised urban dataset preprocessed by SE strategies and comparison algorithms.
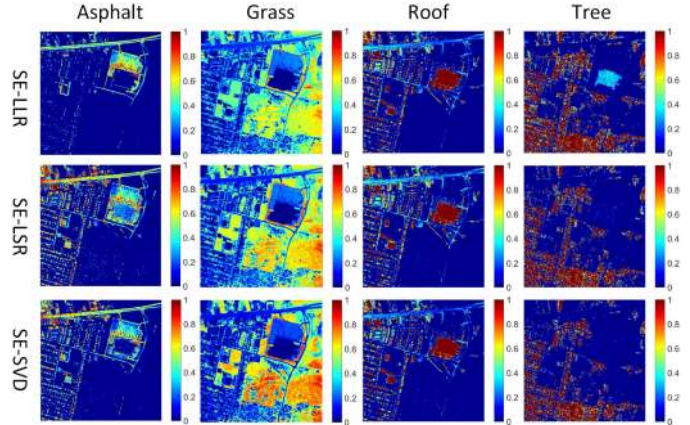

Fig. 13. Qualitative comparison between the fractional abundance maps estimated from the revised urban dataset postprocessed by our proposed SE-LLR, SE-LSR, and SE-SVD.

TABLE VI

COMPARATIVE RESULTS OF OUR PROPOSED SE ALGORITHMS OVER SPECTRAL VARIATION

	Original		Pre-processing+VCA			VCA+Post-processing		
	SPEE	VCA	SE-LLR	SE-LSR	SE-SVD	SE-LLR	SE-LSR	SE-SVD
SAD	0.346	0.275	0.277	**0.274**	0.275	0.560	0.578	0.276
RMSE	**0.002**	0.273	0.248	0.210	**0.002**	0.272	0.272	0.272

reduce the extremely high complexity mainly due to the simplification refine of original image pixels to a subset for subsequent processing.

H. Experiments Over Spectral Variation

In order to further verify that the proposed algorithm can mitigate the effects of spectral variation, a supplementary experiment is conducted. A 100×100 synthetic hyperspectral image used in [35] is adopted in this experiment. In the simulation of this synthetic image, 10 dB Gaussian noises are added to each row of pixels to account for spectral variation within the global area, and additional 50 dB Gaussian noises are added to the pixels inside a block to simulate spectral variation within a local area. We combined the proposed preprocessing and postprocessing SE algorithms with traditional spectral-based VCA algorithm to evaluate the performance of alleviating spectral variation.

The detailed comparative results of the proposed SE algorithms against SPEE and VCA are shown in Table VI. As observed from Table VI, the lowest value of RMSE (shown

noticeable efficiency in improvement of unmixing accuracy. As for real-dataset experiments, the computational preprocessing time of Cuprite is greater than urban HYDICE since the spatial context of Cuprite dataset is much more complex than urban. Moreover, the number of pixels in Cuprite image is larger than urban dataset, which leads to more time being spent on identifying spatially homogenous pixels. While comparing with the SPP under similar principle, it is found that the preprocessing SE-LLR algorithm takes up the same order of magnitude of running time, which also proves the effectiveness of our proposed SE algorithms. On the other hand, RBSPP and RCSPP significantly

TABLE VII
SUMMARY OF THREE PROPOSED SE STRATEGIES

	SE-LLR	SE-LSR	SE-SVD
Exploited SN pixels	all pixels	pixels within homogeneous area	pixels related to greater singular vectors
Solution of weighting factor	least square method	L1 Homotopy method (sparse)	singular value decomposition
Range of application	homogeneous areas	homogeneous and heterogeneous areas	homogeneous and heterogeneous areas
Extra parameter	none	regularization parameter λ	threshold T
Running time	short	longer	long

as coarsening) is achieved by both SPEE and preprocessing SE-SVD. In terms of the SAD, endmembers preprocessed by SE-LSR is more similar to their ground-truth signatures. In general, the proposed SE algorithms could alleviate spectral variation of larger areas, which makes it more effective to find endmembers for SMU. Moreover, preprocessing SE strategies are more effective on eliminating spectral variation than postprocessing in most times. This is because only the spatial context of several selected endmembers are considered in postprocessing SE strategies, rather than all the spatial context of all the pixels in preprocessing SE strategies.

IV. CONCLUSION

In this article, we developed several novel SE strategies, which can be utilized as either a preprocessing step or postprocessing step for the traditional sEF algorithms. Specifically, three preprocessing SE algorithms based on LLR, LSR, and SVD are designed, in which each pixel in a hyperspectral image is modified by exploiting its spatial context. Meanwhile, the proposed spatial-spectral SE strategies can be combined (as a separate module) with any sEF algorithm. A systematical summary of our proposed SE strategies is shown in Table VII. Generally, SE-LSR is better than SE-LLR, especially for the mixing neighborhood consisting of pixels from different classes. This is because only pixels from homogeneous class will help to alleviate spectral variation in SE-LSR while pixels from inhomogeneous classes in a neighborhood may oversmooth centering pixels in SE-LLR. As for SE-SVD, if the threshold is properly settled, its performance will be better than SE-LSR and SE-LLR since spectral variation is alleviated in feature domain. Experiments over both simulated and real hyperspectral data have demonstrated that the proposed SE strategies can clearly improve the performance of sEF algorithms by alleviating local spectral variation using spatial context of pixels, as a preprocessing step or postprocessing step. Moreover, anomalous endmembers can be reserved by simply turning OFF such SE strategy if the pixel is over-smoothed.

In future, we will work toward the automatic identification of anomalous endmembers and integrate this step in SE strategies rather than distinguish all pixels separately. Another direction of efforts is to design endmember identification algorithms to reliably distinguish outliers from anomalous endmembers, so as to retain anomalous endmembers and remove outliers in order to substantiate its potential to improve spectral unmixing techniques. Meanwhile, recent mixture proportion estimation based works [55], [56] also offer a possible solution to enhance the accuracy of estimated fractional abundances.

REFERENCES

[1] Q. Tong, Y. Xue, and L. Zhang, "Progress in hyperspectral remote sensing science and technology in china over the past three decades," *IEEE J. Sel. Topics Appl. Earth Observ. Remote Sens.*, vol. 7, no. 1, pp. 70–91, Jan. 2014.

[2] J. M. Bioucas-Dias, A. Plaza, N. Dobigeon, M. Parente, and J. Chanussot, "Hyperspectral unmixing overview: Geometrical, statistical, and sparse regression-based approaches," *IEEE J. Sel. Topics Appl. Earth Observ. Remote Sens.*, vol. 5, no. 2, pp. 354–379, Apr. 2012.

[3] L. Liu, Y. Lei, and D. Wang, "A fast chaotic image encryption scheme with simultaneous permutation-diffusion operation," *IEEE Access*, vol. 8, pp. 27 361–27 374, 2020.

[4] C. Shi and L. Wang, "Incorporating spatial information in spectral unmixing: A review," *Remote Sens. Environ.*, vol. 149, pp. 70–87, 2017.

[5] J. Plaza and A. Plaza, "Spectral mixture analysis of hyperspectral scenes using intelligently selected training samples," *IEEE Geosci. Remote Sens. Lett.*, vol. 7, no. 2, pp. 371–375, Apr. 2010.

[6] J. Pontius, R. P. Hanavan, R. A. Hallett, B. D. Cook, and L. A. Corp, "High spatial resolution spectral unmixing for mapping ash species across a complex urban environment," *Remote Sens. Environ.*, vol. 199, pp. 360–369, 2017.

[7] C.-I. Chang, W. Xiong, and C.-H. Wen, "A theory of high-order statistics-based virtual dimensionality for hyperspectral imagery," *IEEE Trans. Geosc. Remote Sens.*, vol. 52, no. 1, pp. 188–208, Jan. 2014.

[8] Chang and Chein-I, "A review of virtual dimensionality for hyperspectral imagery," *IEEE J. Sel. Topics Appl. Earth Observ. Remote Sens.*, vol. 11, no. 4, pp. 1285–1305, Apr. 2018.

[9] J. Harsanyi, W. Farrand, and C.-I. Chang, "Detection of subpixel spectral signatures in hyperspectral image sequences," in *Proc. Annu. Meeting, Proc. Amer. Soc. Photogrammetry Remote Sens.*, 1994, pp. 236–247.

[10] C. I. Chang and Q. Du, "Estimation of number of spectrally distinct signal sources in hyperspectral imagery," *IEEE Trans. Geosci. Remote Sens.*, vol. 42, no. 3, pp. 608–619, Mar. 2004.

[11] B.-D. J. M. and N. J. M. P., "Hyperspectral subspace identification," *IEEE Trans. Geosci. Remote Sens.*, vol. 46, no. 8, pp. 2435–2445, Aug. 2008.

[12] D. Heinz and C. Chang, "Fully constrained least squares linear spectral mixture analysis method for material quantification in hyperspectral imagery," *IEEE Trans. Geosci. Remote Sens.*, vol. 39, no. 3, pp. 529–545, Mar. 2001.

[13] S. Mei, M. He, Z. Wang, and D. Feng, "Mixture analysis by multichanel hopfield neural network," *IEEE Geosci. Remote Sens. Lett.*, vol. 7, no. 3, pp. 455–459, Jul. 2010.

[14] A. Plaza, P. Martinez, R. Pérez, and J. Plaza, "A quantitative and comparative analysis of endmember extraction algorithms from hyperspectral data," *IEEE Trans. Geosci. Remote Sens.*, vol. 42, no. 3, pp. 650–663, Mar. 2004.

[15] J. C. Harsanyi and C.-I. Chang, "Hyperspectral image classification and dimensionality reduction: An orthogonal subspace projection approach," *IEEE Trans. Geosci. Remote Sens.*, vol. 32, no. 4, pp. 779–785, Jul. 1994.

[16] J. Boardman, F. Kruse, and R. Green, "Mapping target signatures via partial unmixing of AVIRIS data," in *Proc. Summaries JPL Airborne Earth Sci. Workshop*, 1995, pp. 23–26.

[17] M. Winter, "N-FINDR: an algorithm for fast autonomous spectral endmember determination in hyperspectral data," in *Proc. SPIE, Image Spectrometry V*, 1999, vol. 3753, pp. 266–277.

[18] H. Ren and C.-I. Chang, "Automatic spectral target recognition in hyperspectral imagery," *IEEE Trans. Aerosp. Electron. Syst.*, vol. 39, no. 4, pp. 1232–1249, Oct. 2003.

[19] J. Nascimento and J. Dias, "Vertex component analysis: A fast algorithm to unmix hyperspectral data," *IEEE Trans. Geosci. Remote Sens.*, vol. 43, no. 4, pp. 898–910, Apr. 2005.

[20] C. Chang, C. Wu, W. Liu, and Y. Ouyang, "A new growing method for simplex-based endmember extraction algorithm," *IEEE Trans. Geosci. Remote Sens.*, vol. 44, no. 10, pp. 2804–2819, Oct. 2006.

[21] M. D. Craig, "Minimum-volume transforms for remotely sensed data," *IEEE Trans. Geosci. Remote Sens.*, vol. 32, no. 3, pp. 542–552, May 1994.

[22] J. Li, A. Agathos, D. Zaharie, J. M. Bioucas-Dias, and X. Li, "Minimum volume simplex analysis: A fast algorithm for linear hyperspectral unmixing," *IEEE Trans. Geosci. Remote Sens.*, vol. 53, no. 9, pp. 5067–5082, Sep. 2015.

[23] T.-H. Chan, C.-Y. Chi, Y.-M. Huang, and W.-K. Ma, "A convex analysis-based minimum-volume enclosing simplex algorithm for hyperspectral unmixing," *IEEE Trans. Signal Process.*, vol. 57, no. 11, pp. 4418–4432, Nov. 2009.

[24] L. Miao and H. Qi, "Endmember extraction from highly mixed data using minimum volume constrained nonnegative matrix factorization," *IEEE Trans. Geosci. Remote Sens.*, vol. 45, no. 3, pp. 765–777, Mar. 2007.

[25] S. Mei and M. He, "Minimum endmember-wise distance constrained nonnegative matrix factorization for spectral mixture analysis of hyperspectral images," in *Proc. IEEE Int. Geosci. Remote Sens. Symp.*, Jul. 2011, pp. 1299–1302.

[26] A. Huck, M. Guillaume, and J. Blanc-Talon, "Minimum dispersion constrained nonnegative matrix factorization to unmix hyperspectral data," *IEEE Trans. Geosci. Remote Sens.*, vol. 48, no. 6, pp. 2590–2602, Jun. 2010.

[27] Y. Qian, S. Jia, J. Zhou, and A. Robles-Kelly, "Hyperspectral unmixing via $l_{1/2}$ sparsity-constrained nonnegative matrix factorization," *IEEE Trans. Geosci. Remote Sens.*, vol. 49, no. 11, pp. 4282–4297, Nov. 2011.

[28] Z. Yang, G. Zhou, S. Xie, S. Ding, J. Yang, and J. Zhang, "Blind spectral unmixing based on sparse nonnegative matrix factorization," *IEEE Trans. Image Process.*, vol. 20, no. 4, pp. 1112–1125, Apr. 2011.

[29] J. Li, J. M. Bioucasdias, A. Plaza, and L. Lin, "Robust collaborative nonnegative matrix factorization for hyperspectral unmixing (R-CoNMF)," *IEEE Trans. Geosci. Remote Sens.*, vol. 54, no. 10, pp. 6076–6090, Oct. 2016.

[30] X. R. Feng, H. C. Li, J. Li, Q. Du, A. Plaza, and W. J. Emery, "Hyperspectral unmixing using sparsity-constrained deep nonnegative matrix factorization with total variation," *IEEE Trans. Geosci. Remote Sens.*, vol. 56, no. 10, pp. 6245–6257, Oct. 2018.

[31] Gillis and Nicolas, "Successive nonnegative projection algorithm for robust nonnegative blind source separation," *Siam J. Imag. Sci.*, vol. 7, no. 2, pp. 1420–1450, 2014.

[32] S. Das, A. Routray, and A. Deb, "Convex set based abundance constrained unmixing of hyperspectral image," in *Proc. 14th IEEE India Council Int. Conf.*, Dec. 2017, pp. 1–5.

[33] S. Das, S. Chakraborty, A. Routray, and A. K. Deb, "Fast linear unmixing of hyperspectral image by slow feature analysis and simplex volume ratio approach," in *Proc. IEEE Int. Geosci. Remote Sens. Symp.*, 2019, pp. 560–563.

[34] Z. Shi, T. Shi, M. Zhou, and X. Xu, "Collaborative sparse hyperspectral unmixing using l_0 norm," *IEEE Trans. Geosci. Remote Sens.*, vol. 56, no. 9, pp. 5495–5508, Sep. 2018.

[35] S. Mei, M. He, Z. Wang, and D. Feng, "Spatial purity based endmember extraction for spectral mixture analysis," *IEEE Trans. Geosci. Remote Sens*, vol. 48, no. 9, pp. 3434–3445, Sep. 2010.

[36] A. Plaza, P. Martinez, R. Perez, and J. Plaza, "Spatial/spectral endmember extraction by multidimensional morphological operations," *IEEE Trans. Geosci. Remote Sens.*, vol. 40, no. 9, pp. 2025–2041, Sep. 2002.

[37] D. Rogge, B. Rivard, J. Zhang, A. Sanchez, J. Harris, and J. Feng, "Integration of spatial–spectral information for the improved extraction of endmembers," *Remote Sens. Environ.*, vol. 110, no. 3, pp. 287–303, 2007.

[38] M. Zortea and A. Plaza, "Spatial preprocessing for endmember extraction," *IEEE Trans. Geosci. Remote Sens.*, vol. 47, no. 8, pp. 2679–2693, Aug. 2009.

[39] G. Martin and A. Plaza, "Region-based spatial preprocessing for endmember extraction and spectral unmixing," *IEEE Geosci. Remote Sens. Lett.*, vol. 8, no. 4, pp. 745–749, Jul. 2011.

[40] G. Martin and A. Plaza, "Spatial-spectral preprocessing prior to endmember identification and unmixing of remotely sensed hyperspectral data," *IEEE J. Sel. Topics Appl. Earth Observ. Remote Sens.*, vol. 5, no. 2, pp. 380–395, Apr. 2012.

[41] S. Lopez, J. F. Moure, A. Plaza, G. M. Callico, J. F. Lopez, and R. Sarmiento, "A new preprocessing technique for fast hyperspectral endmember extraction," *IEEE Geosci. Remote Sens. Lett.*, vol. 10, no. 5, pp. 1070–1074, Sep. 2013.

[42] F. Kowkabi, H. Ghassemian, and A. Keshavarz, "A fast spatial-spectral preprocessing module for hyperspectral endmember extraction," *IEEE Geosci. Remote Sens. Lett.*, vol. 13, no. 6, pp. 782–786, Jun. 2016.

[43] F. Kowkabi, H. Ghassemian, and A. Keshavarz, "Enhancing hyperspectral endmember extraction using clustering and oversegmentation-based preprocessing," *IEEE J. Sel. Topics Appl. Earth Observ. Remote Sens.*, vol. 9, no. 6, pp. 2400–2413, Jun. 2016.

[44] X. Xu, J. Li, C. Wu, and A. Plaza, "Regional clustering-based spatial preprocessing for hyperspectral unmixing," *Remote Sens. Environ.*, vol. 204, pp. 333–346, Jul. 2018.

[45] T. Gao, Z. Liu, J. Cao, and S. Liang, "Local difference ternary sequences descriptor based on unsupervised min redundancy mutual information feature selection," *Multidimensional Syst. Signal Process.*, vol. 31, pp. 771–791, 2020.

[46] S. Roweis and L. Saul, "Nonlinear dimensionality reduction by locally linear embedding," *Science*, vol. 290, no. 5500, pp. 2323–2326, 2000.

[47] M. Ma, S. Mei, S. Wan, J. Hou, Z. Wang, and D. D. Feng, "Video summarization via block sparse dictionary selection," *Neurocomputing*, vol. 378, pp. 197–209, 2020.

[48] J. Peng, W. Sun, and Q. Du, "Self-paced joint sparse representation for the classification of hyperspectral images," *IEEE Trans. Geosci. Remote Sens.*, vol. 57, no. 2, pp. 1183–1194, Feb. 2019.

[49] J. Peng, L. Li, and Y. Y. Tang, "Maximum likelihood estimation-based joint sparse representation for the classification of hyperspectral remote sensing images," *IEEE Trans. Neural Netw. Learn. Syst.*, vol. 30, no. 6, pp. 1790–1802, Jun. 2019.

[50] M. Asif and J. Romberg, "Sparse recovery of streaming signals using l1-homotopy," *IEEE Trans. Signal Process.*, vol. 62, no. 16, pp. 4209–4223, Aug. 2014.

[51] S. Danaher and E. O'Mongain, "Singular value decomposition in multispectral radiometry," *Int. J. Remote Sens.*, vol. 13, no. 9, pp. 1771–1777, 1992.

[52] J. Boardman, "Inversion of imaging spectrometry data using singular value decomposition," in *Proc. IEEE Int. Geosci. Remote Sens. Symp.*, 1989, vol. 4, pp. 2069–2072.

[53] J. Boardman, "Geometric mixture analysis of imaging spectrometry data," in *Proc. IEEE Int. Geosci. Remote Sens. Symp.*, vol. 4, 1994, pp. 2369–2371.

[54] S. Mei, M. He, Y. Zhang, Z. Wang, and D. Feng, "Improving spatial-spectral endmember extraction in the presence of anomalous ground objects," *IEEE Trans. Geosci. Remote Sens.*, vol. 49, no. 11, pp. 4210–4222, Nov. 2011.

[55] C. Scott, "A rate of convergence for mixture proportion estimation, with application to learning from noisy labels," in *Proc. 18th Int. Conf. Artif. Intell. Statist. (AISTATS)*, vol. 38, May 2015, pp. 838–846.

[56] H. G. Ramaswamy, C. Scott, and A. Tewari, "Mixture proportion estimation via kernel embedding of distributions," in *Proc. 33rd Int. Conf. Mach. Learn.*, vol. 48, 2016, pp. 2052–2060.

Shaohui Mei (Member, IEEE) received the B.S. degree in electronics and information engineering and the Ph.D. degree in signal and information processing from Northwestern Polytechnical University, Xi'an, China, in 2005 and 2011, respectively.

He is currently an Associate Professor with the School of Electronics and Information, Northwestern Polytechnical University. He was a Visiting Student with the University of Sydney, from 2007 to 2008. His research interests include hyperspectral remote sensing image processing and applications, intelligent signal and information acquisition and processing, video processing, and pattern recognition.

Dr. Mei was the recipient of Excellent Doctoral Dissertation Award of Shaanxi Province in 2014, and Best Paper Award of IEEE ISPACS 2017. He is currently the Reviewer of more than 20 international famous academic journals, and was awarded the Best Reviewer of IEEE JOURNAL OF SELECTED TOPICS IN APPLIED EARTH OBSERVATIONS AND REMOTE SENSING, in 2019. He was the Registration Chair of IEEE China Summit and International Conference on Signal and Information Processing 2014.

Ge Zhang received the B.S. degree in electronics and information engineering, in 2018 from Northwestern Polytechnical University, Xi'an, China, where she is currently working toward the Ph.D. degree in information and communication engineering with the School of Electronics and Information.

Her research interests include hyperspectral image unmixing and signal processing.

Yifan Zhang (Member, IEEE) received the B.S. degree in electron and information technology and the M.S. and Ph.D. degrees in signal and information processing from Northwestern Polytechnical University, Xi'an, China, in 2001, 2004, and 2007, respectively.

From 2007 to 2010, she worked as a Postdoctoral Researcher with the Vision Lab, Department of Physics, University of Antwerp, Antwerp, Belgium. She is currently an Associate Professor with School of Electronics and Information, Northwestern Polytechnical University of China. Her research interests include hyperspectral image analysis, image fusion, and image restoration.

Jun Li (Senior Member, IEEE) received the B.S. degree in geographic information systems from Hunan Normal University, Changsha, China, in 2004, the M.E. degree in remote sensing from Peking University, Beijing, China, in 2007, and the Ph.D. degree in electrical engineering from the Instituto de Telecomunicações, Instituto Superior Técnico, Universidade Técnica de Lisboa, Lisbon, Portugal, in 2011.

She is currently a Full Professor with Sun Yat-sen University, Guangzhou, China. Her main research interests comprise remotely sensed hyperspectral image analysis, signal processing, supervised/semisupervised learning, and active learning.

Prof. Li is an Associate Editor for the IEEE JOURNAL OF SELECTED TOPICS IN APPLIED EARTH OBSERVATIONS AND REMOTE SENSING (since 2014). She has been a Guest Editor for several journals, including the Proceedings of the IEEE and the ISPRS Journal of Photogrammetry and Remote Sensing. She has also been an active reviewer for several journals, including the IEEE TRANSACTIONS ON GEOSCIENCE AND REMOTE SENSING, the IEEE Geoscience and Remote Sensing Letters, the IEEE TRANSACTIONS ON IMAGE PROCESSING, PATTERN RECOGNITION, OPTICAL ENGINEERING, *Journal of Applied Remote Sensing*, and *Inverse Problems and Imaging*. She has received several important awards and distinctions, including the IEEE Geoscience and Remote Sensing Society Early Career Award, in 2017, due to her outstanding contributions to remotely sensed hyperspectral and synthetic aperture radar data processing.

Qian Du (Fellow, IEEE) received the Ph.D. degree in electrical engineering from the University of Maryland at Baltimore County, Baltimore, MD, USA, in 2000.

She is currently the Bobby Shackouls Professor with the Department of Electrical and Computer Engineering, Mississippi State University, MS, USA. Her research interests include hyperspectral remote sensing image analysis and applications, pattern classification, data compression, and neural networks.

Dr. Du is a Fellow of IEEE and the SPIE-International Society for Optics and Photonics. She was a recipient of the 2010 Best Reviewer Award from the IEEE Geoscience and Remote Sensing Society. She was a Co-Chair for the Data Fusion Technical Committee of the IEEE Geoscience and Remote Sensing Society from 2009 to 2013, and the Chair for Remote Sensing and Mapping Technical Committee of the International Association for Pattern Recognition from 2010 to 2014. She served as an Associate Editor of the IEEE JOURNAL OF SELECTED TOPICS IN APPLIED EARTH OBSERVATIONS AND REMOTE SENSING, the *Journal of Applied Remote Sensing*, and the IEEE Signal Processing Letters. Since 2016, she has been the Editor-in-Chief of the IEEE JOURNAL OF SELECTED TOPICS IN APPLIED EARTH OBSERVATIONS AND REMOTE SENSING. She is the General Chair for the 4th IEEE GRSS Workshop on Hyperspectral Image and Signal Processing: Evolution in Remote Sensing in Shanghai, China, in 2012.